

Subsystem relaxation and a calibrated sampling diagnostic for programmable quantum annealers

Luis Lozano

Tecnológico de Monterrey, Campus Santa Fe, Mexico City, Mexico

Programmable quantum annealers are used as open-system samplers, but it is unclear when reverse annealing erases preparation memory and what the readout represents. Here we implement a subsystem–environment protocol on two D-Wave quantum annealers, varying environment size, coupling, disorder, preparation, geometry and QPU generation. A six-qubit subsystem becomes initial-state independent when the environment is large or strongly coupled, while quenched disorder and atypical environment states arrest relaxation. Pairing the memory order parameter with the distance to a calibrated conditional-Boltzmann reference yields a diagnostic that flags rare wrong-basin trapping memory loss alone misses; memory-retaining conditions stay far from the reference (median 0.35). Relaxed ferromagnetic readouts are near-deterministic, so small distances there are a consistency check, not a thermometric test. In a mixed-frustration benchmark, the local-update model practitioners assume mispredicts QPU relaxation roughly sevenfold, whereas non-local classical sampling recovers it. We provide a subsystem-level validation protocol for quantum-annealer sampling.

Introduction

Programmable quantum annealers are increasingly used as open-system samplers for quantum machine learning, hybrid optimization pipelines and the training of Boltzmann machines [1, 2, 3, 4, 5]. For any such workflow, two operational questions are unavoidable: under what conditions does a reverse-anneal protocol erase its initial-state memory, and what distribution does the readout actually represent? A recent review highlights that whether, and under what conditions, a sufficiently large annealer can act as an effective bath for its own subsystems remains experimentally unresolved, and that no controlled study had been performed on annealing hardware [6]. Temperature-estimation, freeze-out and Gibbs-sampling studies have shown that annealer outputs can sometimes resemble effective Boltzmann distributions while also exposing local/global and scale-dependent limitations [7, 8, 9, 10]. Reverse-anneal memory erasure [11], finite-temperature criticality via quantum annealing [12], and programmable localization [13] provide closely related but distinct context, and the theoretical foundations connecting subsystem relaxation to the structure of the global quantum state are well established [14, 15, 16]. What has been lacking is a direct, subsystem-level experimental test in which bath size, coupling, disorder and environment preparation can all be tuned independently on the same programmable platform.

Luis Lozano: lalozanom@tec.mx

Here we provide such a test on two D-Wave QPUs with different topologies and energy scales [17, 18, 19, 20]. We partition the annealer into a small subsystem S ($|S| = 6$) coupled through programmable boundary couplers of strength λ to an on-chip environment E (up to $|E| = 50$), and use reverse annealing with a pause at $s_p = 0.4$ to probe the dynamics. We report a two-observable validation protocol. The memory order parameter \mathcal{M} , defined as the maximum total-variation distance between subsystem marginals from different initial preparations of S , identifies when the subsystem has become initial-state independent. The distance D_{TV} between the measured subsystem readout and a calibrated conditional-Boltzmann reference then acts as a discrepancy detector: large D_{TV} flags relaxed-but-non-thermal trapping that the memory criterion alone cannot detect. We find a tunable crossover from memory retention to relaxation with increasing bath size and coupling, arrest of this crossover by quenched disorder and atypical bath preparations, and a small set of relaxed-but-non-thermal wrong-basin traps isolated by the reference; on relaxed ferromagnetic conditions the readout is near-deterministic and its small distance to the reference is a consistency check rather than a thermometric measurement (it is essentially independent of the calibrated temperature; see Methods and Supplementary Information). A mixed-frustration stress test then exposes a concrete benchmarking failure mode: on Advantage2 the local single-spin-flip Glauber dynamics that annealer users routinely assume underpredicts the QPU relaxation rate roughly sevenfold, whereas non-local classical samplers recover it—so the gap reflects update locality, not quantum dynamics, and is precisely the failure the two-observable diagnostic is built to catch.

We emphasize that D-Wave QPUs operate as open quantum systems: the cryogenic environment, control noise, and the time-dependent anneal schedule itself contribute to the dynamics [21, 20]. The results therefore describe subsystem relaxation during reverse annealing, not thermalization in a strictly isolated system; we make no claim of isolated-system eigenstate thermalization [22, 16], many-body localization [23, 24], or quantum computational advantage. The contribution is a subsystem-level validation protocol for quantum-annealer sampling, controlled by an independently calibrated effective inverse temperature.

Results

Reverse-anneal protocol and subsystem partition

Our experiment uses D-Wave’s reverse-annealing protocol (Fig. 1b). The QPU implements the time-dependent Hamiltonian $H(s) = -\frac{A(s)}{2} \sum_i \sigma_x^i + \frac{B(s)}{2} H_P$, where $H_P = \sum_i h_i \sigma_z^i + \sum_{ij} J_{ij} \sigma_z^i \sigma_z^j$ is the programmable problem Hamiltonian and $s \in [0, 1]$ parameterizes the anneal [25]. In reverse annealing, the system is initialized in a classical state at $s = 1$, ramped to a pause point $s_p < 1$ where quantum fluctuations are reintroduced, held for a pause time t_p , and returned to $s = 1$ for readout.

We partition the qubits into a subsystem S ($|S| = 6$) and an environment E ($|E|$ up to 50), connected through boundary couplers of strength λ (Fig. 1c). Internal couplings are ferromagnetic ($J = -1$), and quenched disorder is introduced as random longitudinal fields $h_i \sim \mathcal{U}[-W, W]$. Different initial preparations of S (all spins up, all down, or random) are used while holding E fixed. The key observable is the memory order parameter \mathcal{M} , defined as the maximum pairwise total variation distance (TVD) between the marginal distributions P_S obtained from different initial states (see Methods). $\mathcal{M} \rightarrow 0$ signals initial-state independence; $\mathcal{M} = 1$ indicates complete memory retention.

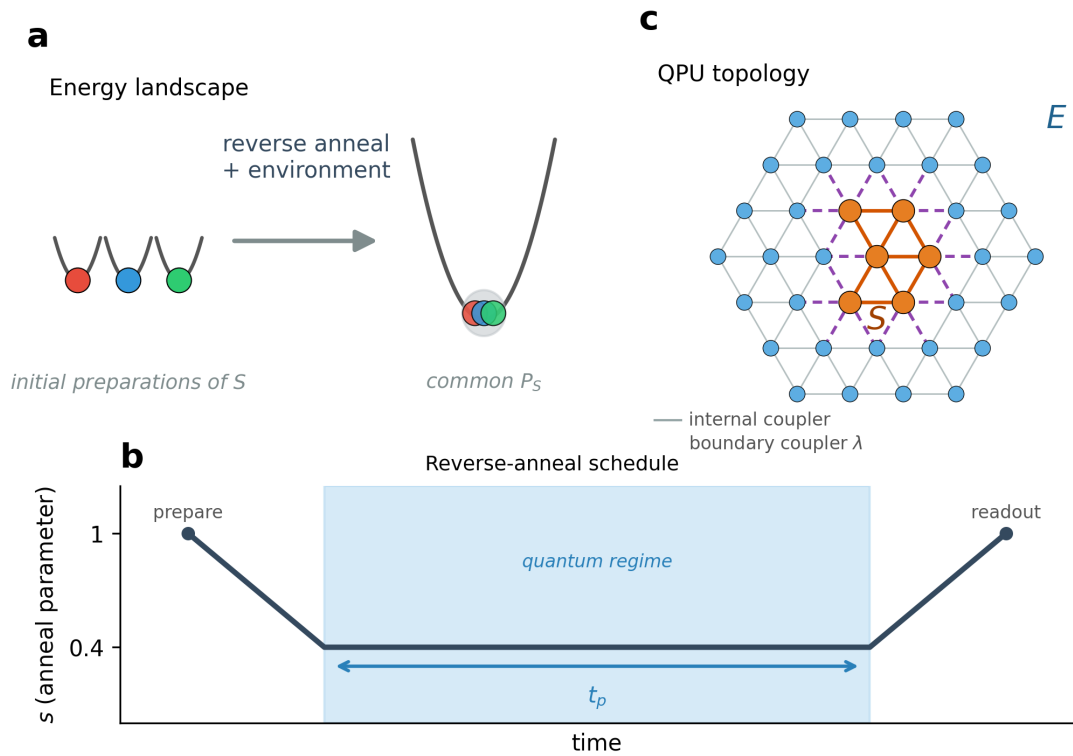


Figure 1: **Reverse-anneal protocol and subsystem–environment partition.** **a**, Energy-landscape concept: three distinct initial preparations of the subsystem (colored balls in different potential wells) converge to the same distribution under relaxing conditions after reverse annealing in the presence of a large on-chip environment. **b**, Reverse-anneal schedule. The system is initialized at $s = 1$ (classical), ramped to a pause point s_p where quantum fluctuations are reintroduced (blue-shaded region), held for a time t_p , and returned to $s = 1$ for readout. **c**, Schematic of the subsystem–environment partition on the QPU topology. The subsystem S (orange, $|S| = 6$) is a connected cluster of qubits; the environment E (blue) surrounds it. Dashed purple lines indicate the boundary couplers of programmable strength λ .

Subsystem relaxation with tunable environment

With the protocol and subsystem partition defined, we first show that enlarging and more strongly coupling the environment drives the subsystem toward initial-state independence within experimental resolution on both QPU generations (Fig. 2). On the Advantage2 QPU ($s_p = 0.4$, $t_p = 100 \mu\text{s}$), the memory order parameter drops sharply with environment size: from $\mathcal{M} = 1.0$ at $|E| = 4$ to $\mathcal{M} = 0.005$ at $|E| = 8$ and $\mathcal{M} < 0.005$ for $|E| \geq 16$ (Fig. 2a, blue circles). The Advantage_system6.4 QPU shows the same qualitative trend, with a slightly higher residual memory at intermediate $|E|$ consistent with its lower energy-to-temperature ratio (Fig. 2a, red squares).

The coupling strength λ provides an independent control parameter (Fig. 2b). On Advantage2, memory decreases monotonically from $\mathcal{M} = 0.94$ at $\lambda = 0.05$ through 0.53 at $\lambda = 0.2$ to $\mathcal{M} < 0.001$ for $\lambda \geq 0.3$. On System 6.4, a similar crossover occurs at lower nominal λ , illustrating that the threshold is platform- and submission-path-dependent rather than set by $\beta_{\text{eff}}\lambda$ alone.

To probe the role of the pause-point Hamiltonian, we sweep s_p on both QPUs (Fig. 2c,d). The crossover curves display the same sigmoidal shape on both platforms: as s_p increases from 0.35 to 0.50, the crossover coupling λ_c shifts to larger values, reflecting the decreasing transverse field. In situ single-qubit probes at $s_p = 0.4$ yield $\beta_{\text{eff}} = 7.22 \pm 0.06$ (Advantage2) and $\beta_{\text{eff}} = 4.29 \pm 0.29$ (System 6.4) (Fig. 3c; see Methods), a ratio of 1.68 consistent with the different hardware energy scales. The common functional form across s_p and the systematic threshold shift between QPUs suggest that pause-point Hamiltonian parameters are important, while platform-specific open-system contributions remain necessary to explain the full crossover; rescaling by $\beta_{\text{eff}}^{\text{S6.4}}/\beta_{\text{eff}}^{\text{A2}} \approx 0.59$ does not produce a single master curve, leaving a residual $\sim 3\times$ gap at $s_p = 0.4$ that is not attributable to the transverse-field ratio $A(s_p)/B(s_p)$ (nearly identical at 0.260 versus 0.259) and is more naturally accommodated by platform-specific open-system contributions (flux-noise spectra, chain strength, calibration epoch, schedule outside the pause) that the dimensionless β_{eff} alone does not capture. The cross-QPU comparison is anchored to a single $(s_p, t_p) = (0.4, 100 \mu\text{s})$ operating point on each device, with t_p set well above the relaxation timescale characterized in the kinetics scan; we did not separately sweep t_p at $s_p = 0.4$ on Advantage_system6.4 (Supplementary Information).

Environment-state dependence and kinetics

We next ask which environment states produce this initial-state independence and on what timescale it develops. At the relaxed working point ($|E| = 50$, $\lambda = 0.5$), an ordered E (all-up or all-down) gives $\mathcal{M} = 0.000$, while a random or domain-wall E leaves residual memory $\mathcal{M} = 0.39$ and 0.65 respectively, with P_S depending on which E preparation was used (cross-preparation TVD = 1.0). The on-chip environment is therefore a finite-size partner whose initial microstate influences the subsystem's fate, not a universal thermal bath. Pause-time kinetics confirm that the ordered/disordered distinction is not a timescale effect: with ordered E , \mathcal{M} drops from 0.017 at $t_p = 1 \mu\text{s}$ to < 0.001 by $t_p = 5 \mu\text{s}$ and remains zero to $t_p = 500 \mu\text{s}$, while with random E it fluctuates between 0.1 and 0.7 over the same range with no systematic decay. We adopt $t_p = 100 \mu\text{s}$ ($\sim 20\times$ the ordered- E relaxation timescale) as the working pause time for all subsequent campaigns. A complementary test using E states produced by forward-annealing the E -only Hamiltonian (with S decoupled), which yields low-energy ordered samples, gives $\mathcal{M} = 0.000$ across the tested preparations, consistent with the expectation [26, 14] that the environment's energy sector controls whether it acts as an effective bath.

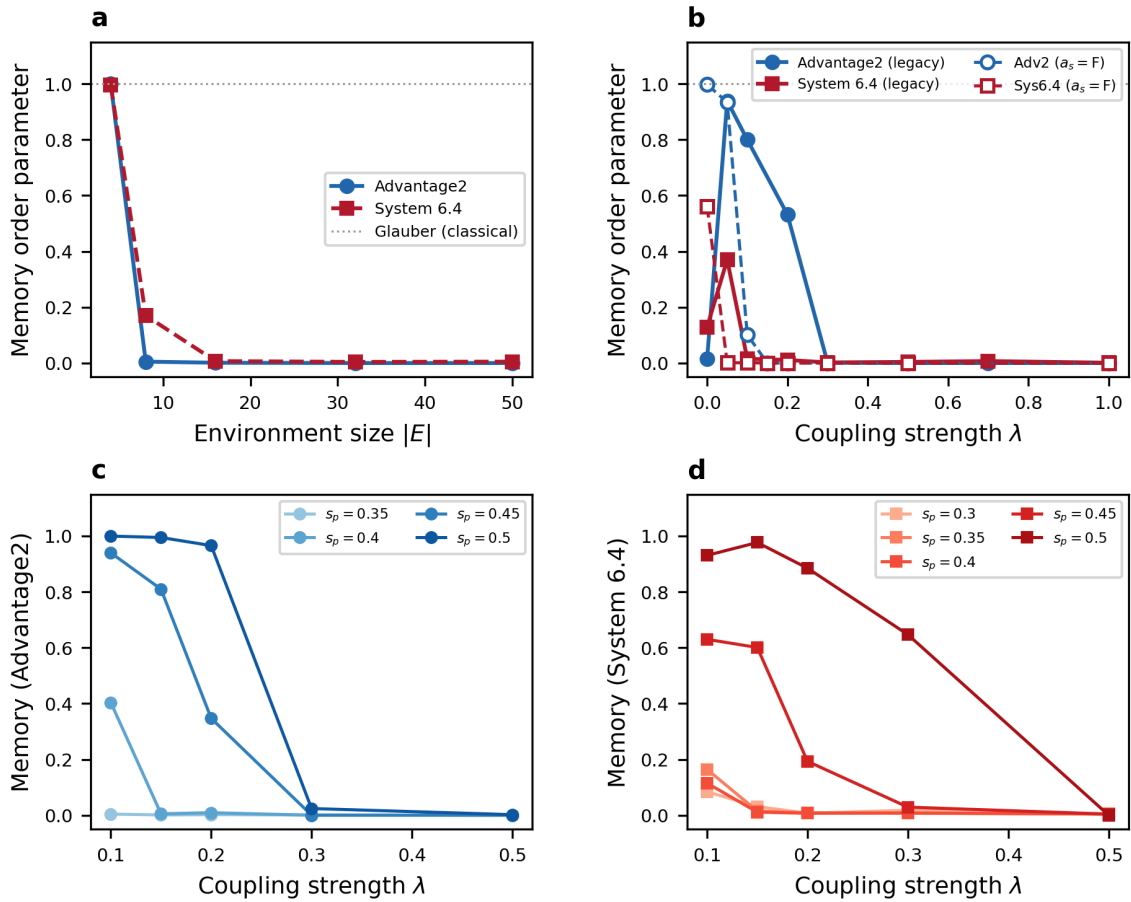


Figure 2: **Subsystem relaxation with tunable environment.** **a**, Memory order parameter \mathcal{M} versus environment size $|E|$ on both QPUs ($s_p = 0.4$, $\lambda = 0.5$). **b**, Memory versus coupling strength λ ($|E| = 50$). Filled markers with solid lines: legacy SDK-default submission path. Open markers with dashed lines: regenerated on direct native-qubit submissions with `auto_scale=False` (no chain couplers). The $\lambda = 0$ point is a decoupled control and is excluded from the monotonic crossover statement. **c,d**, Pause-depth sweeps on Advantage2 (**c**) and System 6.4 (**d**); lower s_p shifts relaxation to weaker coupling. Plotted threshold values are nominal SDK-default quantities and inherit the `auto_scale` systematic characterized in Methods and the Supplementary Information; bootstrap error bars are smaller than the markers unless shown.

Disorder arrests relaxation

The sensitivity to the environment’s initial energy sector suggests that disorder should compete directly with the same relaxation mechanism, which we test by adding random longitudinal fields (Fig. 3a). At fixed $|E| = 50$ and $\lambda = 0.5$, \mathcal{M} remains near zero for $W \leq 1.0$ on both QPUs and then rises to $\mathcal{M} = 0.74$ at $W = 2.0$ on Advantage2 and $\mathcal{M} = 0.50$ at $W = 1.5$ on System 6.4, the lower threshold consistent with its smaller β_{eff} . A five-realization disorder average on Advantage2 gives $\mathcal{M} = 0.000 \pm 0.000$ for $W \leq 1.0$, 0.001 ± 0.001 at $W = 1.5$, and 0.125 ± 0.103 at $W = 2.0$, with the larger spread at $W = 2.0$ reflecting sample-to-sample fluctuations near the crossover. The full (λ, W) crossover diagram on Advantage2 (Fig. 3b, 72 grid points) reveals, at the single system size studied ($|S| = 6$, $|E| = 50$), an empirical boundary separating initial-state-independent and memory-retaining regions, with stronger coupling pushing the disorder threshold higher; absent a finite-size scaling analysis we treat this as a single-size threshold, not a thermodynamic phase boundary. The disorder-arrest threshold is graph-dependent: native Zephyr subgraphs, whose boundary connectivity is roughly an order of magnitude denser than the random 3-regular logical graphs studied here, relax across a broader range of W (Supplementary Information). The lower-connectivity logical graph therefore provides a more stringent test of disorder arrest; the open-system nature of the QPU and the finite pause time preclude direct identification with an MBL transition despite the qualitative resemblance.

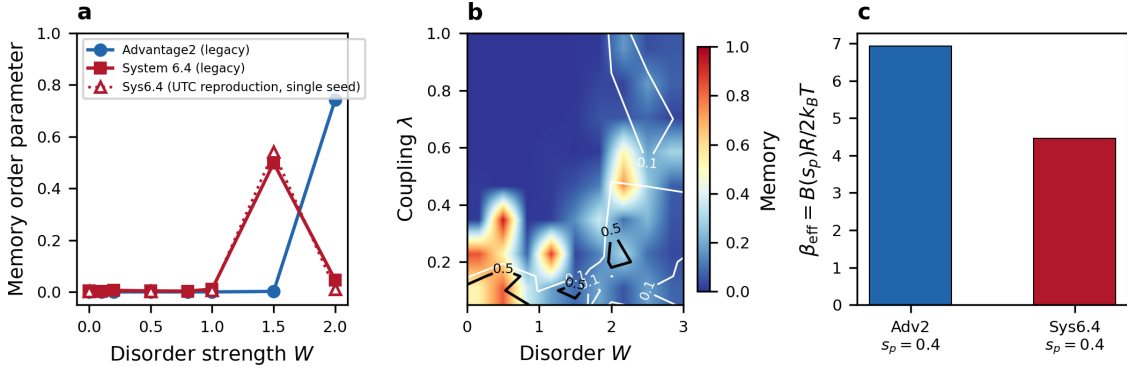


Figure 3: **Disorder arrests relaxation.** **a**, Memory order parameter versus disorder strength W on both QPUs ($|E| = 50$, $\lambda = 0.5$, $s_p = 0.4$). Solid curves: legacy SDK-default submission path. Open triangles (dotted, red): a single-seed reproduction on Advantage_system6.4 at the uniform_torque_compensation chain-strength path with auto_scale=True, giving $\mathcal{M} = 0.54$ at $W = 1.5$ versus the legacy 0.50. Memory rises sharply above $W \approx 1.5$ – 2.0 , indicating disorder-induced arrest of relaxation; the lower threshold on System 6.4 is consistent with its smaller β_{eff} . Smaller fixed chain strengths (Supplementary Information) give weaker arrest, so the arrest magnitude here is specific to the legacy chain-strength regime. **b**, Crossover diagram in the (disorder W , coupling λ) plane on Advantage2 (72 grid points, $|E| = 50$). Color indicates \mathcal{M} ; contour lines at $\mathcal{M} = 0.1$ (white) and 0.5 (black) delineate the relaxed and memory-retaining regions. Stronger coupling pushes the disorder threshold higher. **c**, In situ measured dimensionless energy scale $\beta_{\text{eff}} = B(s_p)R/2k_B T$ at $s_p = 0.4$ on both QPUs.

Calibrated conditional-Boltzmann diagnostic

Having established when the subsystem relaxes, we ask whether the relaxed readout departs from a calibrated reference. We compare the measured marginal P_S with a classical conditional Boltzmann marginal evaluated at an effective inverse temperature calibrated

on independent single-qubit probes. We stress at the outset that this comparison is a *discrepancy detector*, not a thermometer: as shown below, on relaxed ferromagnetic conditions the marginal is near-deterministic and the distance to the reference is essentially independent of the calibrated temperature, so a small distance there is a consistency check rather than a measurement of temperature. The diagnostic earns its value in the opposite regime—large distances reliably isolate non-thermal wrong-basin trapping that the memory criterion alone does not detect.

In-situ β_{eff} calibration. Following classical thermometry for quantum annealers [10], we define β_{eff} as the Boltzmann slope of the z -basis readout distribution produced by the complete reverse-anneal protocol on a single-qubit probe (longitudinal bias $h = 0.5$, same schedule $s_p = 0.4$, $t_p = 100 \mu\text{s}$, `auto_scale=False`, 5,000 reads per initial state),

$$\beta_{\text{eff}} = \frac{1}{2h} \ln \left(\frac{n_{\downarrow}}{n_{\uparrow}} \right), \quad (1)$$

averaged over three probe qubits. This gives $\beta_{\text{eff}} = 7.219 \pm 0.063$ for the main Advantage2 thermal-marginal sweep, $\beta_{\text{eff}} = 7.331 \pm 0.198$ for the separately recalibrated frustrated pilot, and $\beta_{\text{eff}} = 4.289 \pm 0.294$ for the Advantage_system6.4 cross-QPU replication. In every case β_{eff} is a protocol-level readout slope, not a global thermodynamic temperature, and we do not use it to claim a measured temperature of the many-body relaxed state. The reason is explicit and quantified below: sweeping the reference temperature over $\beta \in [\beta_{\text{eff}}/3, 3\beta_{\text{eff}}]$ leaves the relaxed-subset conditional-Boltzmann distance essentially unchanged and far below the sampling floor, the signature of comparing two near-deterministic distributions. β_{eff} therefore serves only to define a fixed reference against which large departures (wrong-basin trapping) are detected; it is not, and is not claimed to be, a fitted many-body temperature.

Conditional Gibbs prediction. For an environment prepared in a fixed ordered state $\sigma_E = \mathbf{1}$, the classical target for the subsystem is the conditional marginal

$$P_S^{\text{th}}(\sigma_S | \sigma_E = \mathbf{1}) = \frac{\exp[-\beta_{\text{eff}} H_P(\sigma_S, \sigma_E = \mathbf{1})]}{\sum_{\sigma'_S} \exp[-\beta_{\text{eff}} H_P(\sigma'_S, \sigma_E = \mathbf{1})]}, \quad (2)$$

evaluated by direct enumeration of the $2^{|S|}$ subsystem configurations with σ_E held fixed. This conditional object differs from the unconditional equilibrium marginal, which would average over both ordered Z_2 sectors and predict zero subsystem magnetization in globally spin-flip-symmetric instances.

Relaxed-subset distances are a consistency check, not a thermometric test. In a 10-seed disorder sweep at $N = 12$, $|S| = 4$, $\lambda = 0.5$ on a 3-regular logical graph (Fig. 4), relaxed conditions sit very close to the conditional classical reference: mean D_{TV} over relaxed realizations lies between 0.6×10^{-3} and 3.6×10^{-3} across $W \in \{0, 0.25, 0.5, 0.75, 1.0, 1.25\}$, with no monotone W dependence (Fig. 4b), while the relaxed fraction decreases from 10/10 at $W = 0$ to 4/10 at $W = 1.25$ (Fig. 4a). These distances are one to two orders of magnitude *below* the multinomial sampling floor (≈ 0.026 for $|S| = 4$, 6,000 reads), which is itself the signature that the relaxed ferromagnetic readout and the reference are both near-deterministic distributions concentrated on the prepared-boundary configuration; we therefore read this as a consistency check, not as a stringent confirmation of the Boltzmann *form*. A direct test makes this explicit: sweeping the reference inverse temperature over

$\beta \in [\beta_{\text{eff}}/3, 3\beta_{\text{eff}}]$ changes the relaxed-subset median D_{TV} only between 1.7×10^{-4} and 3.5×10^{-3} —never approaching the sampling floor—so the agreement does not localize a temperature (Supplementary Information, β -sensitivity). The diagnostic’s discriminating power instead lies in the large-distance regime. Across the full 494-condition Advantage2 sweep (native Zephyr, random 3-regular, three Hamiltonian scales, large-bath native and disorder sub-experiments), 113/494 conditions are relaxed; all but three have conditional $D_{\text{TV}} < 0.05$, and the three exceptions are two severe wrong-basin traps ($D_{\text{TV}} > 0.94$) and one borderline miss described below, while the 381 memory-retaining conditions sit far from the reference (median $D_{\text{TV}} = 0.35$). An independent 60-condition cross-QPU replication on Advantage_system6.4 at the separately calibrated $\beta_{\text{eff}} = 4.29$ gives 22/60 relaxed instances with conditional $D_{\text{TV}} \in [3 \times 10^{-5}, 0.029]$ (median 0.005). The contribution is therefore a two-observable diagnostic—memory loss plus distance to a fixed calibrated reference—that separates ordinary relaxation, relaxed-but-non-thermal wrong-basin trapping, and memory-retaining conditions, across graph geometry, subsystem size $|S| \in \{4, 6\}$, coupling $\lambda \in \{0.2, 0.3, 0.5\}$ and Hamiltonian scale (Fig. 4c); it is not a claim that the relaxed readout is a thermometrically calibrated Boltzmann state.

Quantum reduced Gibbs diagnostic. The same comparison can be repeated with the z -basis diagonal of the quantum reduced Gibbs state of the pause-point Hamiltonian, $H(s_p) = -\frac{A(s_p)}{2} \sum_i \sigma_x^i + \frac{B(s_p)}{2} H_P$, evaluated on the full N -qubit system by exact diagonalization for $N \leq 12$, with the transverse field retained at s_p . We use the same protocol-level β_{eff} and the device-calibrated ratio $A(s_p)/B(s_p) = 0.260$ for Advantage2 and 0.259 for Advantage_system6.4, extracted from the solver anneal-schedule spreadsheets at $s_p = 0.4$. Two quantum targets are compared against the measured marginal: the *conditional* quantum reduced Gibbs marginal with σ_E fixed to the prepared ordered state, and the *unconditional* marginal tracing over all $2^{|E|}$ environment configurations. The unconditional target performs much worse in every ferromagnetic regime (median $D_{\text{TV}} \approx 0.5$ in the Advantage2 disorder sweep) because it averages over both ordered sectors of the global Z_2 and cannot encode the prepared all-up boundary; the conditional target agrees on the disorder sweep (median $D_{\text{TV}} = 0.0145$ across 43 relaxed Advantage2 conditions, 0.0146 across 22 Advantage_system6.4 conditions) but the classical conditional target is uniformly tighter, with the residual gap consistent with the calibrated β_{eff} acting as a post-return-ramp protocol-level readout slope that absorbs the small transverse-field-induced mixing of the pause-point reduced state. Full per-condition D_{TV} tables and the Hamiltonian-scale dependence of the conditional quantum target are reported in the Supplementary Information.

Dynamical-trapping failure modes. Three relaxed conditions in the 494-instance thermal-marginal sweep fail the thermal-marginal test against the classical conditional target at $D_{\text{TV}} > 0.05$ (all three at $\lambda = 0.2$, $N = 8$, $W = 1.0$, native Zephyr subgraph). Two of them are severe wrong-basin failures ($D_{\text{TV}} > 0.94$ classical, > 0.35 quantum conditional) in which the three initial subsystem states converge to nearly the same distribution but that distribution places 98.5% of its weight on the higher-energy all-down basin rather than the all-up ground state at the calibrated β_{eff} , identifying these instances as dynamical trapping into a common non-thermal basin (per-condition values in Supplementary Information). Reporting \mathcal{M} and D_{TV} as two independent quantities separates this failure mode from ordinary relaxation, and also separates ordinary relaxation from the 22/381 memory-retaining conditions whose pooled marginal accidentally resembles the conditional target even though the individual initial-state distributions remain distinct. The classification is

stable under the corrected device-calibrated $A(s_p)/B(s_p)$.

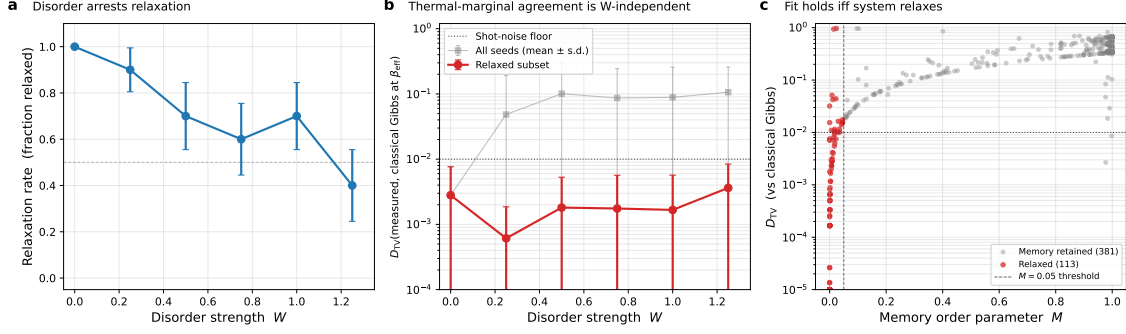


Figure 4: Effective thermal marginal. **a**, Fraction of relaxed disorder realizations ($\mathcal{M} \leq 0.05$) in the 10-seed disorder sweep ($N = 12$, $|S| = 4$, $\lambda = 0.5$, 3-regular logical graph, Advantage2). Relaxation fraction decreases from 10/10 at $W = 0$ to 4/10 at $W = 1.25$. **b**, Total-variation distance between the pooled subsystem marginal and the calibrated classical conditional Gibbs target at $\beta_{\text{eff}} = 7.219$ vs disorder strength. Open circles: all 10 seeds; filled circles: relaxed subset only (error bars = s.d. across relaxed seeds). Gray band: finite-shot reference $D_{\text{TV}} \simeq \frac{1}{2} \sqrt{K/N_{\text{reads}}} \approx 0.026$ with $N_{\text{reads}} = 6000$, $K = 2^{|S|} = 16$; the relaxed subset stays at or below this scale across the sweep. **c**, Scatter of D_{TV} vs \mathcal{M} across all thermal-marginal conditions. Red: relaxed ($\mathcal{M} \leq 0.05$); gray: memory-retaining. Two top-left red outliers correspond to the same $\lambda = 0.2$, $N = 8$, $W = 1$, seed 42 native Zephyr instance at Hamiltonian scales 0.35 and 0.5 (dynamical trapping, discussed in the body). The memory and thermal-marginal criteria identify the same condition set apart from this trapping pair and one borderline $D_{\text{TV}} = 0.051$ miss.

Classical and small-system controls

We next compare the relaxation crossovers and thermal-marginal endpoint against classical and small-system quantum controls (Fig. 5). Single-spin-flip Glauber dynamics at the device effective temperature, and continuous-spin $O(3)$ spin-vector Monte Carlo [27], both give $\mathcal{M} = 1.0$ across the experimental ranges of system size, coupling strength, and disorder (Fig. 5a; Supplementary Information). Exact diagonalization (ED) of the closed quantum Hamiltonian for $N \in \{8, 10, 12\}$ ($|S| = 4$) shows the same qualitative trend as the QPU data: at $s_p = 0.4$, $t_p = 0.5 \mu\text{s}$, \mathcal{M} falls from 0.47 at $N = 8$ to 0.13 at $N = 12$ (Fig. 5b); at $s_p = 0.5$, \mathcal{M} remains above 0.94 at all sizes. A complementary Lindblad master equation with local thermal jump operators at the device temperature reproduces the same qualitative trends (Supplementary Information). While this agreement does not establish that the QPU dynamics are themselves unitary, it is consistent with pause-point transverse-field terms playing an important role in the small-system relaxation [20]. On both QPUs, the threshold coupling λ_c shifts systematically with s_p (Fig. 5c), with deeper pauses producing relaxation at weaker coupling, an s_p dependence that a mechanism governed purely by the classical problem Hamiltonian would not generate (open-system effects including s_p -dependent decoherence may also contribute).

Barrier crossing under mixed frustration

We finally stress-test the diagnostic against classical samplers of differing strength under mixed frustration, introduced by sign-flipping the S couplers with probability p_S (Edwards–Anderson bond disorder) while keeping E ferromagnetic, which produces a multi-modal classical landscape within S while preserving the bath character of E . At

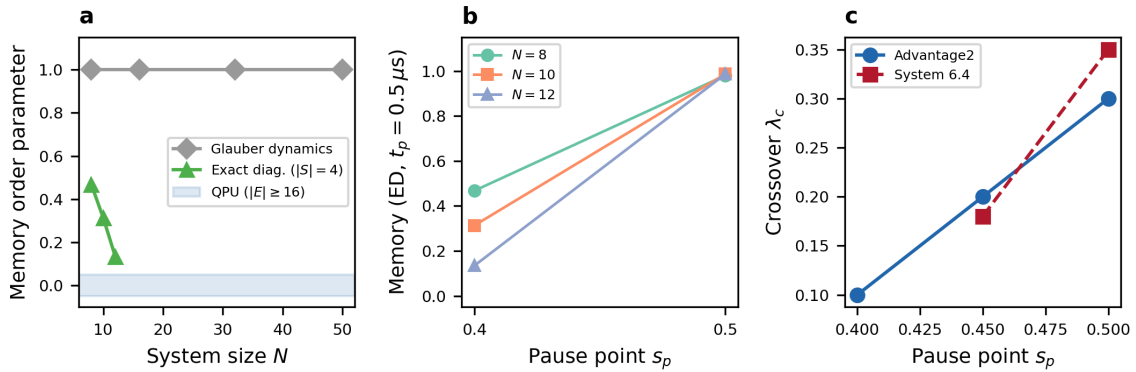


Figure 5: **Classical and small-system controls.** **a**, Comparison across system sizes at fixed $s_p = 0.4$ and representative (λ, W) (see Supplementary Sec. 3 for the full Glauber and SVMC sweeps over system size, coupling strength and disorder). Glauber dynamics at the device temperature (gray diamonds) shows $\mathcal{M} = 1.0$ everywhere. ED at $s_p = 0.4$ (green triangles) shows decreasing memory with system size. The blue-shaded band indicates the QPU result for $|E| \geq 16$ ($\mathcal{M} < 0.01$). **b**, ED memory versus pause depth s_p for three system sizes. Stronger transverse field (lower s_p) drives relaxation; weaker field preserves memory. **c**, Crossover coupling λ_c (approximate nominal thresholds, defined as the λ where \mathcal{M} drops below 0.5) versus pause depth s_p on both QPUs. The plotted λ_c values are nominal logical couplings under the SDK-default submission path and inherit the auto-scale systematic characterized in the Methods and Supplementary Information. The systematic shift with s_p supports the interpretation that the transverse field at the pause point controls the relaxation threshold.

$p_S = 0.5$, $W = 1.0$ ($|S| = 4$, $|E| = 8$, $N = 12$, $\lambda = 0.5$), the QPU relaxes 14/20 instances (70%) on Advantage2 and 10/20 (50%) on Advantage_system6.4. The benchmarking failure mode is sharpest on Advantage2: matched-temperature single-spin-flip Glauber—the local-update reference most commonly assumed for an annealer—relaxes only 2/20 (10%) at $\beta_{\text{eff}} = 7.2$ and needs $T \approx 4.8 \times T_{\text{device}}$ to match, a roughly sevenfold misprediction (Fig. 6a). On System 6.4 the calibrated device temperature is higher and local Glauber is already close to the QPU (45% versus 50%; a weak $1.7\times$ comparison, Fig. 6b), so the strong local-update failure is specifically an Advantage2, low-temperature effect. This gap is a property of update locality, not of quantum dynamics: at the *same* device temperature a non-local classical sampler reproduces the QPU rate—parallel tempering relaxes 13/20 on Advantage2 (65%, 95% CI [0.45, 0.85]) and 11/20 on System 6.4 (55%, [0.35, 0.75]), statistically indistinguishable from the QPU. Parallel tempering was given a 20-replica ladder with 3,600 sweeps per instance—substantially more computational effort per sample than the QPU’s single reverse-anneal read—so this is a statement about local-update *adequacy*, not a like-for-like resource comparison; we make no claim of a nonclassical relaxation pathway (Fig. 6; deposited `pt_sqa_baseline.json`). Exact enumeration of the 2^{12} configurations gives 9.2 local minima on average and a mean energy gap $\Delta = 1.93$, so $\beta_{\text{eff}}\Delta \approx 14$ (Fig. 6c): single-spin-flip activation is exponentially suppressed at the Advantage2 device temperature, whereas replica-exchange moves are not, which accounts for the separation. The practical message stands: a user who treats a reverse-anneal device as equivalent to local thermal dynamics at the calibrated temperature mispredicts relaxation by $\sim 7\times$ in this regime, exactly the failure the two-observable diagnostic is built to expose. Relaxation persists across frustration densities $p_S \in \{0.3, 0.4, 0.5\}$ (per- p_S aggregate 53–64%, 69/120 instances; Supplementary Information). By contrast, full Edwards–Anderson disorder across the entire $S + E$ system produced zero relaxed instances among 463 deposited Advantage2 conditions (lowest $\mathcal{M} = 0.42$), indicating that a fully frustrated environment did not act as a bath under the tested reverse-anneal protocol.

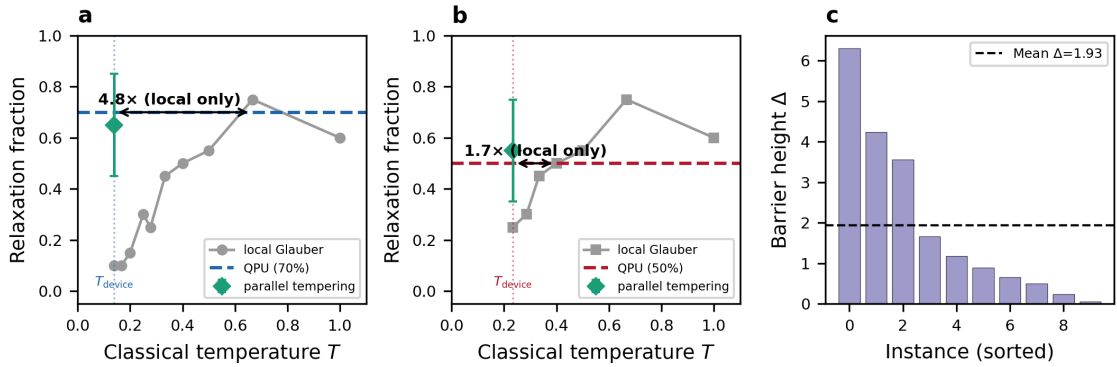


Figure 6: **Non-local classical sampling reproduces the mixed-frustration relaxation gap.** **a**, Relaxation fraction versus classical temperature T on mixed-frustration instances ($p_S = 0.5$, $W = 1.0$, $N = 12$, 20 seeds), Advantage2. Local single-spin-flip Glauber (gray) reaches the QPU rate (blue dashed, 70%) only at $T \approx 4.8 \times T_{\text{device}}$ —a roughly sevenfold misprediction by the local-update model. At the device temperature, parallel tempering (green diamond, 65%; error bar 95% bootstrap CI) reproduces the QPU rate. **b**, Same comparison on Advantage_system6.4: the higher calibrated device temperature leaves local Glauber already close to the QPU (45% vs 50%; a weak $1.7\times$), so the strong local-update failure is specific to the lower-temperature Advantage2 setting. Parallel tempering 55% at T_{device} . **c**, Energy-gap distribution Δ between the global and second-lowest local minimum across ten $N = 12$ frustrated instances (exact enumeration). The mean gap $\Delta = 1.93$ gives $\beta_{\text{eff}}\Delta \approx 14$: single-spin-flip activation is exponentially suppressed at the Advantage2 device temperature, whereas replica-exchange moves are not. Parallel tempering used a 20-replica ladder with 3,600 sweeps per instance, substantially more computational effort per sample than the QPU single read; the comparison establishes local-update *inadequacy*, not a like-for-like resource comparison. QPU rates and the local-Glauber gap use the SDK-default submission path (see Methods); the parallel-tempering baseline is deposited in `pt_sqa_baseline.json`.

Discussion

The two-observable validation protocol introduced here separates *whether* a reverse-anneal subsystem has relaxed from *what* its readout actually represents. Across the 494-condition thermal-marginal campaign on Advantage2, 113 conditions satisfy the relaxation criterion $\mathcal{M} \leq 0.05$; 110 of those agree with the calibrated classical conditional Boltzmann marginal at $D_{\text{TV}} < 0.05$, with the tightest disorder-sweep subset reaching $D_{\text{TV}} \sim 10^{-3}$. The three exceptions are two severe wrong-basin traps and one borderline miss ($D_{\text{TV}} = 0.051$) at $\lambda = 0.2$, $N = 8$, $W = 1.0$, seed 42 on a native Zephyr subgraph; these conditions satisfy the memory criterion but place most of their weight on the higher-energy basin, exposing a relaxed-but-non-thermal failure mode that a single-observable benchmark would not catch. An independent 60-condition cross-QPU replication on Advantage.system6.4 at the separately calibrated $\beta_{\text{eff}} = 4.29$ gives the same qualitative picture (Effective thermal marginal subsection).

Under mixed frustration ($p_S = 0.5$ in S , ferromagnetic E), the sharpest result is a benchmarking failure on Advantage2: the QPU relaxes $\sim 70\%$ of $N = 12$ instances at the calibrated β_{eff} , while matched-temperature single-spin-flip Glauber—the local-update model annealer users routinely assume—relaxes only $\sim 10\%$ and needs $\sim 4.8\times$ the device temperature to match, a roughly sevenfold misprediction. On System 6.4 the higher calibrated temperature leaves local Glauber already close to the QPU (45% versus 50%), so this strong failure is an Advantage2 low-temperature effect rather than a universal one. The separation is a property of update locality, not of quantumness: at the same device temperature parallel tempering reproduces the QPU rate (65% Advantage2, 55% System 6.4), consistent with the exact-enumeration landscape ($\beta_{\text{eff}}\Delta \approx 14$, Arrhenius-suppressed for single-spin-flip but not replica-exchange moves). Parallel tempering used substantially more computational effort per sample than the QPU’s single read, so this is a statement about local-update adequacy, not a like-for-like resource comparison; we explicitly do not claim a nonclassical relaxation pathway. The benchmarking message is the contribution: a user who treats a reverse-anneal device as equivalent to local thermal dynamics at the calibrated temperature mispredicts relaxation by $\sim 7\times$ in this regime—precisely the failure the two-observable diagnostic is built to expose—and an `auto_scale=False` re-verification preserves the qualitative separation within seed variability.

D-Wave QPUs operate as open quantum systems with cryogenic bath, flux noise and time-dependent anneal schedule all participating in the dynamics [21, 20, 19, 28]. The relaxation threshold in $|E|$ characterises the effective boundary-coupling density of the chosen graph family rather than a universal qubit-count threshold: native Zephyr subgraphs, with roughly an order of magnitude denser boundary connectivity, relax at smaller $|E|$ on the same logical problem than the random 3-regular graphs in Fig. 2a; conversely at $|E| = 20$, $\lambda = 0.5$ a direct native-qubit submission remains memory-retaining while the embedded random-3-regular submission at larger $|E| = 50$ relaxes (Supplementary Information). The small relaxed-subset distances persist on the native Zephyr topology (mean conditional $D_{\text{TV}} = 0.0015$ across 5 relaxed conditions, $N = 12$, $|S| = 4$, $\lambda = 0.5$), so the consistency check is not solely an embedding artifact.

The wrong-basin trapping conditions identified by the thermal-marginal test show that initial-state independence alone can mask non-thermal endpoints, an aliasing that single-observable benchmarks do not detect. For annealer-based Boltzmann-machine training [1, 2, 3], quantum-assisted sampling and reverse-anneal optimization [9, 29, 11, 4, 5, 10], we propose reporting \mathcal{M} and D_{TV} against a calibrated β_{eff} alongside any final-energy or success-probability metric, and logging the embedding chain strength, the `auto_scale`

flag, the calibration epoch, and the per-QPU $A(s_p)/B(s_p)$ together with the samples themselves; the calibrated effective temperature alone is not sufficient to interpret the programmed Hamiltonian. The environment-preparation results add a concrete bath-engineering principle: ordered, low-energy auxiliary qubits act as effective baths, whereas random, domain-wall or fully frustrated environments arrest relaxation, so bath qubits should be initialized deliberately rather than allowed to relax alongside the problem region.

Looking ahead, a bath-ensemble experiment with multiple certified low-energy environment microstates would strengthen the effective-bath interpretation beyond ordered boundary conditions; a larger frustrated campaign with native topologies would test whether the local-update separation persists at larger N ; and a systematic study of the cross-QPU collapse residual against noise spectra and embedding could turn the β_{eff} -only failure mode into a dynamical calibration tool. Beyond sampling and optimization, the same controlled subsystem-bath protocol turns programmable annealers into testbeds for open-system quantum simulation at scales that exceed exact diagonalization, complementing the cold-atom and trapped-ion platforms where comparable experiments are limited to tens of qubits [30, 31, 32]. In addressing the open question of [6], our results show that a sufficiently large annealer can act as an effective bath for its own subsystems under ordered low-energy environment preparations (all sizes studied at $N \leq 12$ and $|S| \in \{4, 6\}$), that this bath-like behavior is arrested by disorder and atypical environment states in sparse embedded geometries, and that a fixed calibrated conditional-Boltzmann reference, used as a discrepancy detector rather than a thermometer, cleanly separates relaxed, relaxed-but-trapped, and memory-retaining readouts on both QPU generations—a transferable benchmarking protocol for annealer-as-sampler workflows rather than a thermalization claim.

Methods

Quantum processing units

Experiments were performed on two D-Wave QPUs [33]: the Zephyr-topology Advantage2 (4,579 active qubits, operated as `Advantage2_system1.13` for the sweeps of Figs. 2–3 and 5, then `Advantage2_system1` with qubit 4374 removed for the thermal-marginal and mixed-frustration campaigns of Figs. 4 and 6) and the Pegasus-topology Advantage_system6.4 (5,612 active qubits) for the cross-QPU replication. The dimensionless energy scale $\beta_{\text{eff}} = B(s_p)R/2k_B T$ (with $B(s_p)$ the problem energy scale at the pause point, R the `auto_scale` rescaling factor, and T the physical device temperature) was measured in situ by submitting single-qubit probes at $h = 0.5$ under the full reverse-anneal protocol ($s_p = 0.4$, $t_p = 100 \mu\text{s}$, `auto_scale=False`, 5,000 reads), extracting $\beta_{\text{eff}} = \ln(n_{\downarrow}/n_{\uparrow})/(2h)$ averaged over three probe qubits from the solver nodelist. This procedure gives $\beta_{\text{eff}} = 7.219 \pm 0.063$ for the Advantage2 thermal-marginal campaign and $\beta_{\text{eff}} = 4.289 \pm 0.294$ for the Advantage_system6.4 cross-QPU replication; the frustrated pilot uses an independently recalibrated $\beta_{\text{eff}} = 7.331 \pm 0.198$ from a separate run. β_{eff} is a protocol-level readout slope, not a refrigerator temperature: each value is a single per-campaign single-qubit-probe calibration, not verified for cross-calibration-epoch stability, and it is used only to define a *fixed* conditional-Boltzmann reference for the discrepancy detector, not as a fitted many-body temperature. The relaxed-subset distance to this reference is essentially independent of β_{eff} over a ninefold range (Effective thermal marginal subsection; Supplementary β -sensitivity), so the diagnostic does not rely on the precise value or on temperature drift between sessions. The per-QPU anneal-schedule

coefficients used in the quantum reduced Gibbs diagnostic were extracted from the solver schedule spreadsheets [33], giving $A(s_p)/B(s_p) = 0.260$ for Advantage2 and 0.259 for Advantage_system6.4 at $s_p = 0.4$. Solver rename and qubit-availability dates and full per-campaign metadata are recorded in the Supplementary Information and in the deposited archive.

Hamiltonian family and embedding

The problem Hamiltonian is a random 3-regular Ising model: $H_P = \sum_i h_i \sigma_z^i + \sum_{\langle ij \rangle} J_{ij} \sigma_z^i \sigma_z^j$, with internal couplings $J_{ij} = -1$ (ferromagnetic), boundary couplings between S and E scaled by $\lambda \in [0, 1]$, and quenched disorder $h_i \sim \mathcal{U}[-W, W]$. The main environment-size, coupling, disorder and pause-depth sweeps (Figs. 2–5) use $|S| = 6$ with $|E|$ up to 50; the thermal-marginal and mixed-frustration campaigns use $|S| = 4$ small-system instances at $N \leq 12$ to permit exact classical and quantum reference computations. S is a connected subgraph in all cases. Logical graphs were embedded with `EmbeddingComposite` [34] at the default `uniform_torque_compensation` chain strength; chain-break effects, embedding-induced sampling bias and the Zephyr-vs-Pegasus chain-strength differences are discussed in [35] and in the Supplementary Information.

Reverse-anneal protocol

All experiments use a four-point reverse-anneal schedule [25]: $(0, 1.0) \rightarrow (5 \mu\text{s}, s_p) \rightarrow (5 + t_p \mu\text{s}, s_p) \rightarrow (10 + t_p \mu\text{s}, 1.0)$, with `reinitialize_state=True`. Default parameters: $s_p = 0.4$, $t_p = 100 \mu\text{s}$, 1,000–2,000 reads per configuration. Unless otherwise stated, initial states of S were varied (all-up, all-down, random) while E was initialized all-up; the environment-preparation controls (all-down, random, domain wall, forward-annealed) and the bath-ensemble and frustrated sub-experiments use the preparations described in the Results and Supplementary Information. The submission path differs across sub-experiments and is important for the interpretation of absolute threshold values. The thermal-marginal β_{eff} calibration probes and native-Zephyr thermal-marginal conditions were submitted with `auto_scale=False` on direct physical-qubit submissions so that the programmed and nominal (h, J) coincide. Discovery sweeps, main subsystem-bath sweeps (Figs. 2–5) and the mixed-frustration working point (Fig. 6) were submitted through the SDK-default path with the minor-embedding composite and automatic Hamiltonian rescaling (`auto_scale=True`) both active [33]. We characterized this rescaling through paired `auto_scale`-on/off spot-checks at six embedded and unembedded working points, a transition-region λ -scan, four independent random spin-reversal gauges, and an `auto_scale=False` re-verification of the barrier-crossing working point on both QPUs (Supplementary Information). Outside the transition region the two settings agree exactly or within $|\Delta\mathcal{M}| \lesssim 0.11$, with most saturated points agreeing at 0 or 1, and gauge-averaged \mathcal{M} has standard deviation ≤ 0.02 across gauges at every tested condition; a deposited Advantage_system6.4 `auto_scale=False` re-verification (7/10) and an Advantage2 job-log summary (8/10, not preserved in the present deposit; see Supplementary) preserve the qualitative QPU–Glauber separation, with the exact temperature-gap ratio varying with seed set and Glauber-sweep protocol. Inside the transition region the rescaling shifts the effective crossover in λ in a reproducible manner, so the absolute λ_c values in Figs. 2 and 5 and the temperature-gap ratios in Fig. 6 are reported as empirical quantities for the SDK-default submission path used in the legacy campaigns, not as universal numbers; the public code release defaults to `auto_scale=False`.

Observables and statistical analysis

The marginal distribution $P_S(\sigma_S) = \sum_{\sigma_E} P(\sigma_S, \sigma_E)$ is computed from QPU samples by projecting onto the subsystem qubit indices, using the variable ordering returned by the sampler. The memory order parameter is $\mathcal{M} = \max_{a,b} \text{TVD}(P_S^{(a)}, P_S^{(b)})$, where $\text{TVD}(P, Q) = \frac{1}{2} \sum_x |P(x) - Q(x)|$. Uncertainty estimates on \mathcal{M} are obtained by bootstrap resampling (200 resamples with replacement from the QPU reads), and are used for the error bars shown in the main-text figures; per-condition bootstrap standard deviations and disorder-averaged dispersions are tabulated in the Supplementary Information.

Classical baselines

Glauber dynamics: single-spin-flip Monte Carlo with acceptance probability $p = [1 + \exp(\Delta E/k_B T)]^{-1}$ at the device effective temperature; 10,000 sweeps, 2,000 samples after equilibration. *Exact diagonalization*: the transverse-field Ising Hamiltonian $H(s_p)$ was constructed as a sparse matrix for $N \leq 12$ and time-evolved via `expm_multiply` (SciPy). The schedule coefficients $A(s_p)$ and $B(s_p)$ in GHz are absorbed into $H(s_p)$ directly, and the physical pause time t_p (in μs) is converted to the dimensionless time argument of $\exp(-iHt)$ via $t_{\text{nat}} = 2\pi \times 10^3 t_{\mu\text{s}}$, where the factor of $2\pi \times 10^3$ reconciles GHz with inverse microseconds (in units where $\hbar = 1$). Subsystem marginals were obtained by tracing out environment degrees of freedom. *Spin-vector Monte Carlo*: continuous O(3) Heisenberg spins with Metropolis updates on the unit sphere, using $H = \sum_i h_i n_i^z + \sum_{ij} J_{ij} (\mathbf{n}_i \cdot \mathbf{n}_j)$ and z -axis projected measurement. Full details of all baselines are in the Supplementary Information.

Data availability

The raw D-Wave sampleset data, per-condition metadata (solver identifier, `graph_id`, calibration epoch and timing blocks; embedding information is recorded separately in per-campaign metadata), processed pooled subsystem marginals, the bootstrap resamples used for error bars, the thermal-marginal comparison artifacts, the D-Wave per-QPU anneal-schedule coefficients used for the quantum reduced Gibbs diagnostic, and figure source data for Figs. 2–6 are available to editors and referees through a confidential review-only repository link supplied in the submission package. The complete archive will be made public through a Zenodo record at a citable DOI upon publication.

Code availability

During peer review, custom code central to the reported analyses is made available to editors and referees through a confidential review-only repository link supplied in the submission package; credentials, private account configuration and nonessential operational logs are not included. The repository comprises the reverse-anneal driver, the subsystem-marginal analysis pipeline, the thermal-marginal comparison scripts, the baseline and comparison solvers (Glauber dynamics, exact diagonalization, Lindblad evolution, continuous-spin Monte Carlo, and parallel tempering), and the figure-generation scripts used to produce Figs. 1–6 and all supplementary figures, together with a `pyproject.toml` recording the Ocean SDK and Python package versions used for the experiments. Upon publication, a curated release sufficient to reproduce the reported analyses and figures will be made publicly available on GitHub and archived at Zenodo at a citable DOI, under a license permitting readers to repeat the reported results.

LLM disclosure

LLM-based coding assistants were used for code scaffolding and language editing. All scientific decisions, code validation, data analysis, and interpretation were performed and verified by the author.

Author contributions

L.L. conceived the study, designed the experiments, implemented the software, performed the QPU submissions and classical simulations, analyzed the data, prepared the figures, and wrote the manuscript.

Competing interests

The author declares no competing interests.

Correspondence

Correspondence should be addressed to L.L. (lalozanom@tec.mx).

Acknowledgments

This work received no external financial funding. QPU access was provided through the D-Wave Leap developer platform; D-Wave had no role in study design, data analysis, interpretation, or manuscript preparation. The author thanks the D-Wave support and training teams for platform access and technical assistance with the Leap environment.

References

- [1] Steven H. Adachi and Maxwell P. Henderson. “Application of quantum annealing to training of deep neural networks”. Preprint at <https://arxiv.org/abs/1510.06356> (2015).
- [2] Mohammad H. Amin, Evgeny Andriyash, Jason Rolfe, Bohdan Kulchytskyy, and Roger Melko. “Quantum Boltzmann machine”. *Physical Review X* **8**, 021050 (2018).
- [3] Marcello Benedetti, John Realpe-Gómez, Rupak Biswas, and Alejandro Perdomo-Ortiz. “Estimation of effective temperatures in quantum annealers for sampling applications: A case study with possible applications in deep learning”. *Physical Review A* **94**, 022308 (2016).
- [4] Jon Nelson, Marc Vuffray, Andrey Y. Lokhov, Tameem Albash, and Carleton Coffrin. “High-quality thermal Gibbs sampling with quantum annealing hardware”. *Physical Review Applied* **17**, 044046 (2022).
- [5] Marc Vuffray, Carleton Coffrin, Yaroslav A. Kharkov, and Andrey Y. Lokhov. “Programmable quantum annealers as noisy Gibbs samplers”. *PRX Quantum* **3**, 020317 (2022).
- [6] Viv Kendon and Nicholas Chancellor. “Quantum annealing and condensed matter physics”. *Journal of Physics: Condensed Matter* **38**, 143005 (2026).
- [7] Jack Raymond, Sheir Yarkoni, and Evgeny Andriyash. “Global warming: Temperature estimation in annealers”. *Frontiers in ICT* **3**, 23 (2016).

- [8] Jeffrey Marshall, Eleanor G. Rieffel, and Itay Hen. “Thermalization, freeze-out, and noise: Deciphering experimental quantum annealers”. *Physical Review Applied* **8**, 064025 (2017).
- [9] Jeffrey Marshall, Davide Venturelli, Itay Hen, and Eleanor G. Rieffel. “Power of pausing: Advancing understanding of thermalization in experimental quantum annealers”. *Physical Review Applied* **11**, 044083 (2019).
- [10] George Grattan, Pratik Sathe, and Cristiano Nisoli. “Classical thermometry of quantum annealers” (2025). [arXiv:2512.03162](https://arxiv.org/abs/2512.03162).
- [11] Elijah Pelofske and Cristiano Nisoli. “Erasing classical memory with quantum fluctuations: Shannon information entropy of reverse quantum annealing”. Preprint at <https://arxiv.org/abs/2509.10927> (2025).
- [12] Gianluca Teza et al. “Finite-temperature criticality through quantum annealing” (2025). [arXiv:2507.07167](https://arxiv.org/abs/2507.07167).
- [13] Jaime L. C. da C. Filho, Zoe Gonzalez Izquierdo, Andreia Saguia, Tameem Albash, Itay Hen, and Marcelo S. Sarandy. “Localization transition induced by programmable disorder”. *Physical Review B* **105**, 134201 (2022).
- [14] Sandu Popescu, Anthony J. Short, and Andreas Winter. “Entanglement and the foundations of statistical mechanics”. *Nature Physics* **2**, 754–758 (2006).
- [15] Sheldon Goldstein, Joel L. Lebowitz, Roderich Tumulka, and Nino Zanghì. “Canonical typicality”. *Physical Review Letters* **96**, 050403 (2006).
- [16] Luca D’Alessio, Yariv Kafri, Anatoli Polkovnikov, and Marcos Rigol. “From quantum chaos and eigenstate thermalization to statistical mechanics and thermodynamics”. *Advances in Physics* **65**, 239–362 (2016).
- [17] Andrew D. King, Sei Suzuki, Jack Raymond, Alex Zucca, Trevor Lanting, Fabio Altomare, Andrew J. Berkley, et al. “Coherent quantum annealing in a programmable 2,000 qubit Ising chain”. *Nature Physics* **18**, 1324–1328 (2022).
- [18] Andrew D. King, Jack Raymond, Trevor Lanting, Richard Harris, Alex Zucca, Fabio Altomare, Andrew J. Berkley, et al. “Quantum critical dynamics in a 5,000-qubit programmable spin glass”. *Nature* **617**, 61–66 (2023).
- [19] Vrinda Mehta, Hans De Raedt, Kristel Michielsen, and Fengping Jin. “Unraveling reverse annealing: A study of D-Wave quantum annealers”. *Physical Review A* **112**, 012414 (2025).
- [20] Vrinda Mehta et al. “Understanding the physics of D-Wave annealers: From Schrödinger to Lindblad to Markovian dynamics”. *Physical Review A* **112**, 032616 (2025).
- [21] Tameem Albash and Daniel A. Lidar. “Adiabatic quantum computation”. *Reviews of Modern Physics* **90**, 015002 (2018).
- [22] Marcos Rigol, Vanja Dunjko, and Maxim Olshanii. “Thermalization and its mechanism for generic isolated quantum systems”. *Nature* **452**, 854–858 (2008).
- [23] Rahul Nandkishore and David A. Huse. “Many-body localization and thermalization in quantum statistical mechanics”. *Annual Review of Condensed Matter Physics* **6**, 15–38 (2015).
- [24] Dmitry A. Abanin, Ehud Altman, Immanuel Bloch, and Maksym Serbyn. “Colloquium: Many-body localization, thermalization, and entanglement”. *Reviews of Modern Physics* **91**, 021001 (2019).

- [25] D-Wave Quantum Inc. “D-Wave ocean software documentation: Reverse annealing”. <https://docs.dwavequantum.com> (2024). Accessed 2026.
- [26] Noah Linden, Sandu Popescu, Anthony J. Short, and Andreas Winter. “Quantum mechanical evolution towards thermal equilibrium”. *Physical Review E* **79**, 061103 (2009).
- [27] Seung Woo Shin, Graeme Smith, John A. Smolin, and Umesh Vazirani. “How “quantum” is the D-Wave machine?”. Preprint at <https://arxiv.org/abs/1401.7087> (2014).
- [28] Connor Aronoff, Travis Howard, David Nicholaeff, Alejandro Lopez-Bezanilla, and Wade DeGottardi. “Identifying quantum coherence in quantum annealers” (2026). [arXiv:2602.21355](https://arxiv.org/abs/2602.21355).
- [29] Huo Chen and Daniel A. Lidar. “Why and when pausing is beneficial in quantum annealing”. *Physical Review Applied* **14**, 014100 (2020).
- [30] Adam M. Kaufman, M. Eric Tai, Alexander Lukin, Matthew Rispoli, Robert Schittko, Philipp M. Preiss, and Markus Greiner. “Quantum thermalization through entanglement in an isolated many-body system”. *Science* **353**, 794–800 (2016).
- [31] J. Smith, A. Lee, P. Richerme, B. Neyenhuis, P. W. Hess, P. Hauke, M. Heyl, D. A. Huse, and C. Monroe. “Many-body localization in a quantum simulator with programmable random disorder”. *Nature Physics* **12**, 907–911 (2016).
- [32] Adam L. Shaw, Daniel K. Mark, Joonhee Choi, Ran Finkelstein, Pascal Scholl, Soonwon Choi, and Manuel Endres. “Experimental signatures of hilbert-space ergodicity: Universal bitstring distributions and applications in noise learning”. *Physical Review X* **15**, 031001 (2025).
- [33] D-Wave Quantum Inc. “D-Wave system documentation: Solver properties, anneal schedules and qpu-specific parameters”. https://docs.dwavequantum.com/docs/latest/doc_physical_properties.html (2024). Accessed 2026.
- [34] Jun Cai, William G. Macready, and Aidan Roy. “A practical heuristic for finding graph minors”. Preprint at <https://arxiv.org/abs/1406.2741> (2014).
- [35] Jeffrey Marshall, Andrea Di Gioacchino, and Eleanor G. Rieffel. “Perils of embedding for sampling problems”. *Physical Review Research* **2**, 023020 (2020).